Chapter 3

Structural Characterization of Lithium Niobate Nanoparticles Prepared by the Sol-Gel Process, Using X-Ray and Raman Spectroscopy and Scanning Electron Microscopy

Pedro R.S. Prezas and Manuel P.F. Graça

Additional information is available at the end of the chapter

http://dx.doi.org/10.5772/64395

Abstract

The widespread use of lithium niobate (LN) in several technological applications, notably in optical and electrooptical systems, is a consequence of its remarkable piezoelectric, electrooptical, photoelastic, acousto-optic, and nonlinear optical coefficients. In this chapter, the structural and electrical characterization of LN nanosized particles synthesized by the Pechini route is discussed. Compared to solid-state reaction processes, wet chemistry processes can be advantageous alternatives for the synthesis of polycrystalline LN, because they require lower processing temperatures, and thus the loss of stoichiometry and formation of secondary phases can be minimized. The powders obtained by drying the gel (base powder) were heat-treated for 4 h at temperatures between 400 and 1000°C, according to the differential thermal analysis (DTA) results. It was found that the powders sintered at 450°C contain only the LN phase, while those heat-treated at 500°C already contain the secondary $LiNb_3O_8$ phase. The structural and electrical characterization of the samples sintered at 450°C, for different times, was performed using X-ray diffraction (XRD) in conjunction with Rietveld refinement, Raman spectroscopy, scanning electron microscopy (SEM), and impedance spectroscopy in the temperature range between 200 and 360 K and in the frequency range between 100 Hz and 1 MHz and by measuring the ac and dc conductivities.

Keywords: lithium niobate, structural properties, X-ray spectroscopy, Raman spectroscopy, electrical properties, lithium triniobate, sol-gel process

1. Introduction

Lithium niobate ($LiNbO_3$, LN) is a well-known artificially synthesized ferroelectric material with considerable technological importance, being in competition with barium titanate ($BaTiO_3$, BTO) in several high-tech applications. In fact, an inspection of the number of publications related with LN and BTO will show that since the mid-1990s, the number of reports on both materials has been following the same increasing trend, with similar number of publications, reinforcing the importance of LN among the scientific communities. **Table 1** displays some of the main physical properties of single-crystalline LN [1].

Melting temperature (°C)	1260
Curie temperature (°C)	1210
Density at RT (g/cm^3)	4.64
Refractive index (ordinary), n_0	2.296
Electrooptical coefficient, r_{33} (m/V)	30×10^{-12}
Transparency window (μm)	0.4–5
Resistivity, ρ (c-axis) (Ω cm)	$\log \rho = (7150/T) - 2.823$ (at RT) = 10^{21}
Dielectric constant at RT (ε')—c-axis	80 (100 kHz) >1000 (1 kHz)
Dielectric loss at RT (tan δ)—c-axis	≈0 (100 kHz)
Coercive field (at 1210°C) (V/m)	20
Spontaneous polarization at RT (P_s [$\times 10^{-2}$ C m^{-2}])	70
Piezoelectric coefficient (d_{33} [pC/N])	6
Thermal conductivity at RT (W m^{-1} K^{-1})	3.92

Table 1. Main physical properties of single-crystalline stoichiometric LN. RT stands for room temperature (generally 300 K) [1–3].

LN single crystals display several excellent properties, such as high piezoelectric, electrooptical, photoelastic, acousto-optic, and nonlinear optical coefficients. They are known to have very low acoustic losses, offering a great versatility as a substrate for integrated optic systems: a considerable number of optical devices have been developed based on LN, such as wave guides, surface acoustic wave (SAW) devices, electrooptical wavelength filters and polarization modulators, nonlinear frequency converters (frequency doubling and second harmonic generation), nonvolatile memories, and ultrafast optical processing systems. Its combination of electrooptical and photogalvanic effects makes it photorefractive without the need of applying an external electrical field, thus being able to be applied in holographic data storage. It offers also the possibility of being easily doped, in a controllable way, with optical-active ionic species, using standard techniques such as ion implantation or thermal diffusion.

http://dx.doi.org/10.5772/64395

The physical properties aforementioned are optimized for the case where LN is grown as a single crystal and with stoichiometric composition. Regarding the stoichiometry, LN has a relatively broad composition range, and therefore, it can be labeled as congruent lithium niobate (cLN, 48.35–48.6 mol% Li_2O) and stoichiometric (sLN, ~50 mol% Li_2O). **Figure 1** displays the phase diagram of the Li_2O-Nb_2O_5 binary system, showing the possibility of growing pure LN crystals by using 50% up to ~52% of Nb_2O_5. It also shows the transition of ferroelectric phase to paraelectric by increasing the synthesis temperature and Nb_2O_5 content. The large majority of LN single crystals are grown by the conventional Czochralski method, which yields cLN single crystals. Some competitor methods have been developed for growing stoichiometric crystals, including the vapor transport equilibration (VTE) method, which is a post-grown procedure [4]. The former is more suitable for thin and small samples, because for larger and thicker crystals, very large solid-state diffusion times are required for the Li/Nb ratio equilibration. To attain larger stoichiometric single crystals, more direct growth methods can be applied, such as the double crucible Czochralski method with an automatic power supply [5, 6] or the high-temperature top-seeded solution growth (HTTSSG) method from the K_2O-Li_2O-Nb_2O_5 ternary mixture, which is the one capable of yielding compositions closest to 50 mol% Li_2O [5, 7].

The nonlinear and photorefractive properties will generally degrade with the loss of stoichiometry and consequent increase of defects and impurity density. As a matter of fact, the congruent composition range is regarded as having an intrinsic defect structure which is dominated by lithium vacancies, known as the lithium vacancy model, which translates in Eq. (1) [6]:

$$[Li_{Li}]_{1-5x}[Nb_{Li}]_x[V_{Li}]_{4x}Nb_{Nb}O_3 \quad (1)$$

In this model, as depicted in Eq. (1), for every four lithium vacancies created, a niobium ion occupies a lithium network site, assuring electrical charge neutrality. The cLN is not suitable for high-temperature applications, because degradation processes can start to occur for temperatures starting from 300°C [6, 8]. On the other hand, studies show that sLN can be stable

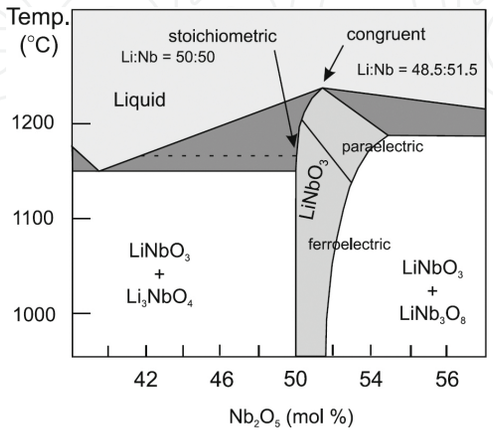

Figure 1. Phase diagram of the Li_2O-Nb_2O_5 binary system [3].

up to temperatures of at least 900°C [6, 9], because some properties like the electrical conductivity do not change under thermal cycling up to such temperatures.

As it was aforementioned, the dominant process in the growth of LN single crystals is the Czochralski method. However, this method is known for its technical and economic drawbacks, as well as being time-consuming. Thus, alternative preparation processes have been researched and explored. Solid-state reaction processes generally require high processing temperatures (>1000°C), which lead to the loss of lithium by evaporation [10]. As a consequence, secondary crystalline phases such as Li_3NbO_4 and $LiNb_3O_8$ can be formed, changing the stoichiometry and deteriorating the properties. Wet chemistry methods, such as sol-gel methodologies and hydrothermal methods, can be good alternatives because they require lower processing temperatures, such as calcination and thermal-sintering treatments, and thus the formation of secondary phases can be minimized [10, 11]. Single crystals in the nanometer and micrometer size ranges can be synthesized at low temperatures, such as 240°C, by these methods [11]. When such methods are applied, typically polycrystalline LN samples are produced, i.e., a material composed by small single crystals in the micrometric or nanometric range randomly distributed with no evident preferential orientation. Polycrystalline LN finds a lot of applications, especially as thin films for integrated optic applications, although generally the properties of polycrystalline materials are not as good as their single-crystalline counterpart. For example, the piezoelectric properties of polycrystalline LN are inferior to the single crystal, and in the best case, they might approach them if all of its domains are perfectly orientated. Further, relative to single-crystalline thin films, the grain boundaries in polycrystalline films may lead to increased light scattering and larger optical losses in wave guides, which may reduce their utility and potentiality in some applications [12]. However, their production is cheaper and easier compared with the growth processes for single crystals, and all these cons and drawbacks have to be considered and well balanced for potential applications.

Amorphous LN is also important for some applications. In an amorphous material, there is no long-range order, and the network can be described as distorted unitary cells randomly oriented. LN single crystals and polycrystals have low electrical conductivity (~10^{-12} S/cm at 500 K for single crystals [13]), and ionic diffusion or mobility is reduced in these materials. However, the amorphous structure is always a more open structure compared with the crystalline composition or, in other words, has a smaller density, which promotes and facilitates the ionic diffusivity, making them suitable for technical application such as solid-state electrolytes for Li-ion batteries. In fact, the reported activation energies for the ionic diffusivity are considerably smaller (half in the 25–150°C temperature range [13]) in amorphous LN.

In this chapter, the structural and electrical characterization of $LiNbO_3$ nanosized particles prepared by the Pechini route, also known in the sol-gel methodologies as the polymeric precursor route, is discussed. The powders obtained by drying the gel (base powder) were heat-treated for 4 h at temperatures between 400 and 1000°C, according to the differential thermal analysis (DTA) results. The sintering temperature revealed to be, as expected, an important parameter in controlling the development of secondary crystalline phases, and it was found that the powders sintered at 450°C contain only the LN phase, while those heat-

http://dx.doi.org/10.5772/64395

treated at 500°C already contain the secondary $LiNb_3O_8$ phase. Their structural characterization was performed using X-ray diffraction (XRD) in conjunction with Rietveld refinement, Raman spectroscopy, and scanning electron microscopy (SEM). The grains observed have sizes lower than 100 nm and an approximately spherical geometry. The electrical characterization of pellets made from the base powder heat-treated at 450°C was made by measuring the dc and ac conductivities and measuring the complex impedance (Z^*) in the temperature range between 200 and 360 K and in the frequency range between 100 Hz and 1 MHz. From the measured complex impedance values, the complex permittivity (ε^*) was calculated, since the geometrical characteristics of the pellets legitimate the use of the parallel plate capacitor model. The correlation between the structure and morphology with the electrical and dielectric properties is one of the main topics of the present chapter.

2. Structural, morphologic, and electrical properties

2.1. Structural properties

LN belongs to a group of materials whose crystalline structure is a perovskite. This structure has the typical chemical formula ABO_3, where the cation A usually is too large for an effective complete packaging, causing a distortion in the unit cell and leading to a displacement of the O^{2-} anions from their expected sites. However, in the case of LN, the distortion is related with the small radius of the lithium ion. For temperatures lower than 1415 K, which is the Curie temperature (T_c) of sLN, this material is in its ferroelectric state, and consequently, it exhibits a spontaneous polarization, due to a nonuniform charge distribution of the lithium and niobium ions. In this ferroelectric phase, this material has a trigonal crystalline structure, with threefold rotation symmetry around its c-axis. **Figure 2(a)** and **(c)** shows the atomic model of LN in its ferroelectric crystalline phase. In this configuration, the crystalline structure consists in layers of oxygen atoms parallel to each other with the Li^+ and Nb^{5+} cations lying along the

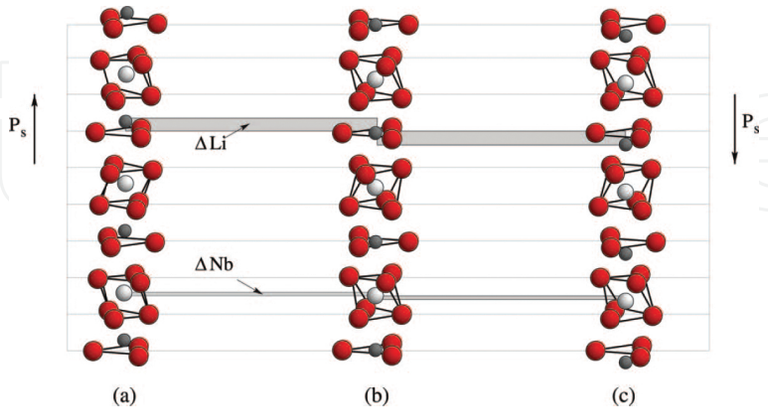

Figure 2. (a) and (c) Atomic model of the LN ferroelectric phase. (b) Atomic model of the LN paraelectric phase. ΔLi indicates the displacement along the c-axis of the Li^+ cations, represented as black spheres, while ΔNb indicates the displacement along the c-axis of the Nb^{5+} cations. Both displacements are represented relatively to the center of the oxygen (red spheres) planes [14].

c-axis, surrounded by oxygen octahedra: in the unitary cell, one-third of the octahedral interstices are occupied by Li^+ cations; another one-third by Nb^{5+} cations and the remaining (one-third) interstices are structural voids [2, 14].

As depicted in **Figure 2**, in the ferroelectric state, the displacement of the Li^+ and Nb^{5+} cations relatively to the center of the oxygen planes originates a spontaneous polarization along the c-axis with a magnitude of 0.7 C/m^2 at 300 K (see **Table 1**). The displacement can be up or down with respect to the oxygen sublattice, and both cations are displaced in the same direction because of the Coulomb repulsion. Above the Curie temperature, due to the thermal expansion of the crystalline lattice axes, the structure is no longer distorted, because the Li^+ and Nb^{5+} cations move to lattice sites lying in the planes of the oxygen layers, as **Figure 2(b)** displays. Thus, the transition to the paraelectric state occurs, and LN ceases to exhibit a permanent spontaneous polarization [2, 14].

As it was stated in Section 1, polycrystalline LN is also of great technological importance. In this form, the structure can be described as composed by small single crystals in the micrometric or nanometric range randomly distributed with no evident preferential orientation. Relatively to the ferroelectricity, it is composed by several ferroelectric domains, which are regions with different orientations of the spontaneous polarization *Ps*. In this case, the thermodynamic potential for describing the ferroelectric phase transition has to account with a nonuniform *Ps* distribution, organized in domains, and therefore the domain depolarization energy W_E and the energy of the domain walls W_W are introduced in the potential [3].

The thermodynamic model for the single-crystal case, an "ideal" ferroelectric, does not need to include the former energy terms W_E and W_W and can be described by Eq. (2) [3]:

$$G(P,T) = G_0 + \frac{\alpha(T)}{2}P^2 + \frac{\beta(T)}{4}P^4 \tag{2}$$

This model is based on the second-order phase transition as described by Landau-Ginsburg; with at least a fourth-order polynomial in *P*, the polarization. *G*(*P*,*T*) is the Gibbs function, and α and β are second- and fourth-order expansion temperature-dependent terms. As it was said, this rather simple form applies for the case when *Ps* is uniform for all the material, as in the case of a single crystal. In the ferroelectric/paraelectric phase transition, the behavior of the plots of the type *G*(*P*,*T*) versus *P*, for different temperatures, is shown in **Figure 3** [3]. As it can be seen, for T_2 and T_{0}, there is only one minimum, while for T_1, in the ferroelectric phase, two minimum values exist, which correspond to the values of the spontaneous polarization *Ps* (can be positive or negative, according to the direction—**Figure 2**). These values can be determined by solving the differential $(\partial G/\partial P)_{Ps} = 0$, resulting in $Ps = \pm\sqrt{\frac{-\alpha}{\beta}}$ for temperatures lower than T_c and $Ps = 0$ for temperatures higher than T_c [3]. The parameters α and β are related with the dielectric constants of LN, and more specifically, α can be expressed above T_c, in the paraelectric phase, according to the Curie-Weiss law shown in Eq. (3) [3, 15]:

http://dx.doi.org/10.5772/64395

$$\chi = \frac{1}{\alpha} = \frac{C}{T - T_c} \tag{3}$$

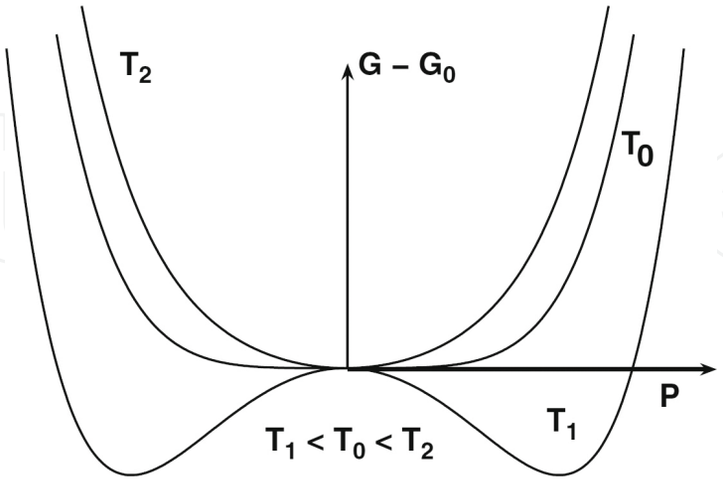

Figure 3. The Gibbs free energy in function of the polarization *P*. T_0 is equal to T_c, and the quantitative relation between the temperatures is $T_1 < T_0 < T_2$ [3].

where χ is the dielectric susceptibility and *C* is a material-dependent constant.

The above-considered model fails when predicting quantities such as the coercive field, both for congruent and stoichiometric LN, because the inversion mechanisms of *Ps* occur through the formation of ferroelectric domains and the model does not account with *Ps* discontinuities. However, this thermodynamic model can be improved to better characterize a ferroelectric material containing domains, according to Eq. (4) [3]:

$$G(P,T) = G_0 + \int_V \left[\frac{\alpha}{2}P^2 + \frac{\beta}{4}P^4 + \frac{1}{2}\delta(\nabla P)^2\right] dV + W_E + W_W \tag{4}$$

As it was stated, the terms depolarization energy W_E and the energy of the domain walls W_W are here introduced. The integration volume, W_E and W_W depend on the domain structure and geometry. In [3] the W_E and W_W expressions are described for a simple periodic domain structure model. The manipulation of the structure and geometry of the domain walls in a ferroelectric such as LN was, and still is, an important subject of study, because depending on the technological application, some geometries/shapes may be preferred over others: for example, acoustic and optical frequency conversion devices will benefit with periodic gratings of antiparallel domains [15]. The domain shape will depend on the temperature at which they are created, through the application of external electric fields and also on the crystal stoichiometry/composition. When created at room temperature, they can show different shapes due to small variation of stoichiometric composition [15]. **Figure 4** shows the preferred shapes of domains created at 25 and 125°C, for a congruent LN. It is visible that the domains have a polygonal shape with six sides, known as *y* walls. Curiously, the domain shape as depicted in **Figure 4(a)** is the same for stoichiometric LN, while in other ferroelectric materials such as $LiTaO_3$, the same does not happen [15].

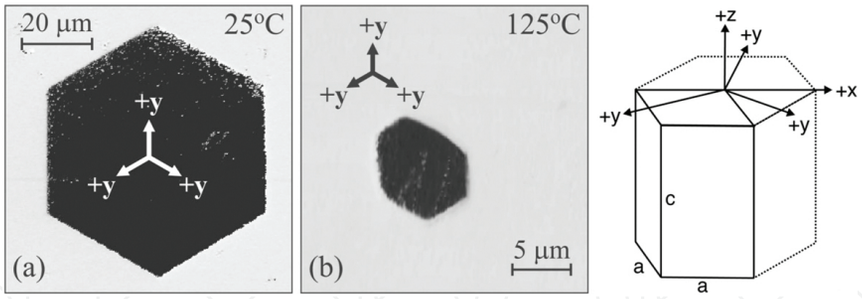

Figure 4. Piezoelectric force microscopy phase contrast images obtained in a congruent LN. The domains were created at 25 and 125°C [15].

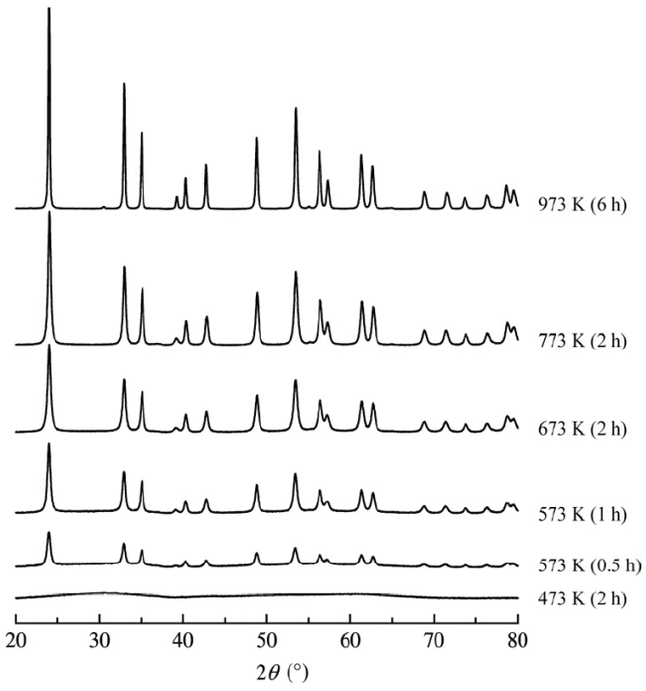

Figure 5. XRD spectra revealing the effect of heat treatments on amorphous LN prepared by complete hydrolysis of the LN double alkoxide [16].

As for the structure of amorphous LN, it was said that the network can be described as distorted unitary cells randomly oriented. **Figure 5** reveals the effect of heat treatments (HTs) on amorphous LN prepared by complete hydrolysis of the LN double alkoxide [16]. The XRD spectra of amorphous LN have the typical form of the spectrum for 473 K displayed in **Figure 5**, with two broad bands around 30 and 50–60°. These broad bands are a trademark of amorphous materials, and they are typically visible for diffraction angles where the crystalline phase has the most intense diffraction peaks, revealing at least a short-range-order preservation. The heat treatments promote the reconfiguration of the amorphous phase to a more thermodynamically stable crystalline phase; although for low treatment temperatures and times, the material may be composed by a heterogeneous mixture of an amorphous and a crystalline phase: for the heat treatment at 573 K for 0.5 h, it is still noticeable the coexistence

http://dx.doi.org/10.5772/64395

of a broad band with the diffraction peaks of the LN crystalline phase [16]. The structure of amorphous LN was also described by Kitabatake et al. to be constructed from the network of NbO_6 octahedra which contains a micronetwork similar to crystalline LN [17]. The high dielectric constant and a relaxation mechanism were attributed to the high mobility of the Li^+ ion in the LN structure [17].

Going further on the structural properties, the Raman spectroscopy is a useful nondestructive technique to access about the structure and composition of materials. The Raman spectrum of LN will generally depend on its stoichiometry, i.e., the shape, width, and position of some Raman shifts may change according to the Li/Nb ratio [18]. Furthermore, the Li/Nb ratio of a given LN sample may be determined by analyzing the width of some Raman lines, for a given temperature [18, 19].

Figure 6 exhibits experimental full width at half maximum (FWHM) values of the Raman lines detected at about 153 and 876 cm^{-1}, for samples with different lithium contents (mol%) [19]. The measurements were carried out at room temperature (note that the Raman lines' width also depends on the temperature). The FWHM dependency with the Li content is approximately linear, and hence a calibration line can be obtained. The uncertainty related with the Li content determination by this method was calculated to be 0.05 mol%, with an estimated uncertainty of 0.2 cm^{-1} in the 876 cm^{-1} line FWHM and 0.1 cm^{-1} in the 153 cm^{-1} line [19]. Therefore, this technique can be a simple nondestructive method to estimate the Li/Nb ratio in LN crystals, with an excellent accuracy.

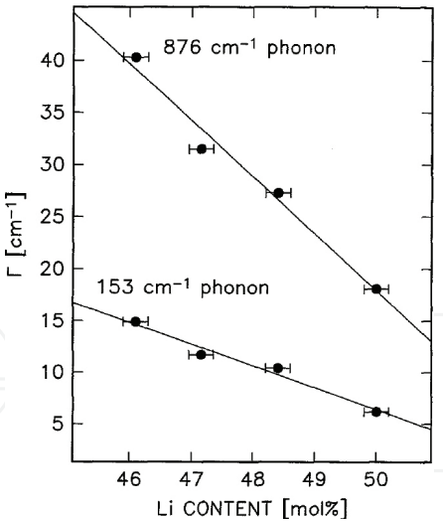

Figure 6. Full width at half maximum of the Raman lines at the wavenumbers 153 and 876 cm^{-1}. The dots are experimental values obtained for samples with different lithium contents (mol%), at room temperature, and the lines are the linear least-squares fits [19].

Figure 7 displays the Raman spectra of a nearly stoichiometric LN crystal, with x_c = 49.7 %, and a congruent LN crystal with x_c = 48.5 %, where x_c is given by $x_c = \frac{[Li]}{[Li]+[Nb]} \times 100\,(\%)$ [18]. According to the group theory, when belonging to the *R3c* spatial group, eighteen vibrational

modes are to be expected, which can be reduced in the representation $4A_1 + 9E + 5A_2$ [18]. The A_2 vibrational modes are not active in Raman and FTIR (silent modes), while both A_1 and E modes are active in Raman and FTIR. The A_1 modes are polarized along the Z-axis, while the E modes represent vibrations along the X- and Y-axes (see **Figure 4**). Therefore, in the XYZ coordinate system, as indicated in **Figure 7**, Z-axis lies in the c-axis direction while the X-axis in the *a*-axis crystallographic direction. The Y-axis is perpendicular to Z and X. The notation represented in the same figure is a universally used notation first described by Damen et al. For example, in X(YZ)Y, the symbols inside the parenthesis are, from left to right, the polarization of the incident and scattered light, while the ones outside the parenthesis, from left to right, represent the directions of the incident and scattered light, respectively [20]. As depicted in **Figure 7**, the E(TO) transversal modes can be detected in the X(ZY)Z configuration, while E(TO) and E(LO) can be detected in both X(ZY)Z and X(YZ)Y configurations [18]. The A_1(TO) phonons, represented in **Figure 7**, at right, can be detected in the X(ZZ)Y configuration. The spectra clearly show that there is a broadening of the lines in the congruent composition, relatively to the nearly stoichiometric, i.e., the nearly stoichiometric spectrum lines are more resolved. Furthermore, there are lines that are only clearly visible in the nearly stoichiometric LN, and thus vibrational mode attribution in congruent LN can be an incomplete task [18]. As a final remark, when dealing with polycrystalline LN, the discussion about the different possible configurations to detect different vibrational modes is not applicable, since in the polycrystalline sample, we have nano- or micrometric single crystals randomly oriented, and thus interaction volume of the laser beam with the sample will include all these different orientations. In Section 2.4, the case study, we include the Raman spectra of polycrystalline LN, where a typical overlapping of vibrational modes is visible. The overlapping is due to the fact that, as **Figure 7** shows, some of the E(TO + LO) and A_1(TO) vibration modes are in the same wavenumber range, and consequently, they will overlap in the polycrystalline LN samples.

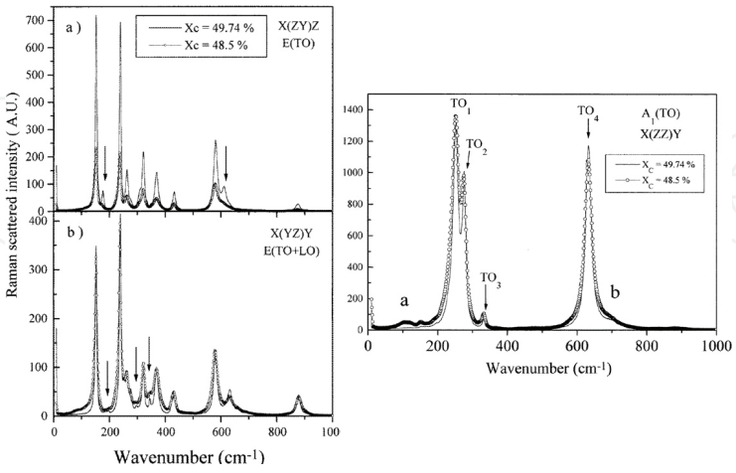

Figure 7. At left: Raman spectra of two LN crystals with composition x_c = 49.7 % (nearly stoichiometric) and x_c = 48.5 % (congruent), exhibiting the E(TO) and E(LO) vibrational modes. The arrows highlight lines that are more clearly visible in the nearly stoichiometric composition. At right: the configuration X(ZZ)Y allows the detection of the A_1(TO) phonons [18].

http://dx.doi.org/10.5772/64395

2.2. Morphological characteristics

Morphology means "the study of form or pattern," and morphological characterization techniques, such as scanning electron microscopy (SEM) or transmission electron microscopy (TEM), allow to characterize the morphology of a given material. The morphological characteristics of LN will obviously rely upon the synthesis process, stoichiometry, and concentration of intrinsic defects. Depending on the synthesis process and crystal growth conditions, the grains observed for polycrystalline LN can display well-defined symmetries and a different range of sizes.

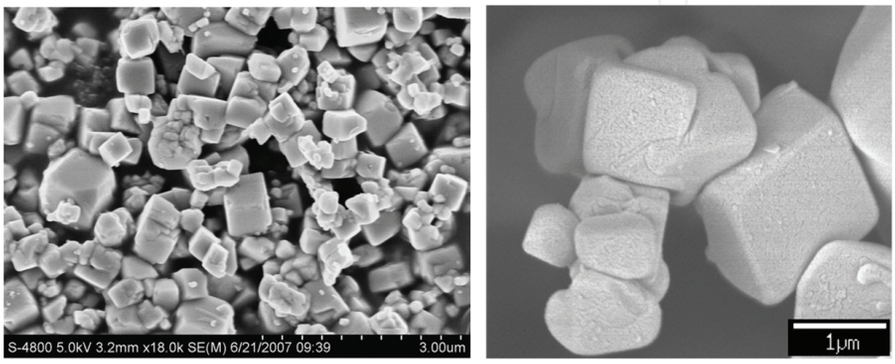

Figure 8. At left: SEM micrograph of polycrystalline LN prepared by a low-temperature hydrothermal route [21]. At right: SEM micrograph of polycrystalline LN prepared by the reactive molten salt synthesis (RMSS) process [10].

Zhan et al. [21] report in their work a low-temperature hydrothermal route to prepare polycrystalline LN. The XRD characterization revealed the formation of a pure hexagonal single phase of stoichiometric LN. The SEM micrograph of the LN powder, presented in **Figure 8**, shows a regular rhombohedral grain morphology, in agreement with the XRD results, although some imperfections, such as bended surfaces, are visible. The grain size ranges from 300 nm to approximately 1 μm. Kamali et al. [10] prepared polycrystalline LN using a modification of the molten salt synthesis (MSS): in conventional MSS, the mixed powders are heated above the liquids' temperature of the salt mixture, and this molten salt acts as the reaction medium, remaining inert during the synthesis. Salt mixtures such as KCl-NaCl are typically used. In the MSS modification approached by [10], the salt can react with other reagents during the synthesis process, being labeled as reactive molten salt synthesis (RMSS). They heat-treated at 973 K Nb_2Cl_5 powder in a LiCl molten salt, in a water-containing atmosphere, whereby the molten salt is one of the precursors for LN synthesis [10]. Using this RMSS approach, they produced single-phased LN, i.e., the loss by evaporation of Li_2O was avoided. A SEM micrograph of the obtained LN particles is shown in **Figure 8**, on the right side [10]. The revealed morphology shows grains with dimensions ranging from several hundreds of nanometers to a few micrometers. The rhombohedral symmetry is also visible, although cleavages and bends are visible.

In **Figure 9**, it is visible a TEM bright-field micrograph of the polycrystalline LN prepared by the RMSS process. The inset on the right top shows a selected area electron diffraction pattern, being the area marked by the black arrow. The diffraction pattern is consistent with single-

crystalline rhombohedral LN. The inset on the left bottom shows a high-resolution micrograph of the area marked by the white arrow. The rhombohedral LN (104) atomic plane patterns are visible, with an interplanar spacing of 0.27 nm [10].

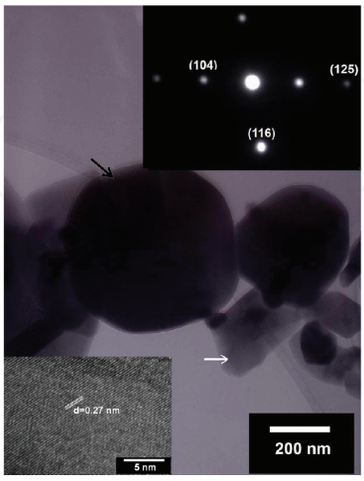

Figure 9. TEM bright-field micrograph of the LN particles prepared by the reactive molten salt synthesis (RMSS). Inset on the top right: selected area electron diffraction pattern of the area marked by the black arrow. Inset on the left bottom: high-resolution micrograph of the area marked by the white arrow [10].

The grain morphology will be determined by the growth conditions in such a way that the final morphology reflects the configuration with the minimum surface energy. In crystalline solid materials, the surface tension will depend on the crystallographic planes and direction, because to create a new surface, it is necessary to break bonds. At a constant pressure and temperature, the work required to create a new portion of surface dA_s in a one-component system is given by Eq. (5) [22]:

$$dW_{T,p} = \gamma dA_s \tag{5}$$

where γ is the surface energy (J/m^2). This represents an excess of energy relatively to the bulk and will depend on the number of bonds of the surface (crystallographic plane) and their bond energy. The change of the Gibbs free energy can be written according to Eq. (6) [22]:

$$dG = -SdT + Vdp + \gamma dA_s \tag{6}$$

where γ is defined as in Eq. (7) [22]:

$$\gamma = \left(\frac{\partial G}{\partial A_s}\right)_{T,P} \tag{7}$$

The formation of new surfaces leads to a positive Gibbs energy contribution, whereby smaller particles will be unstable when compared with larger particles. The equilibrium morphology

http://dx.doi.org/10.5772/64395

of the crystal will be determined by the surfaces with lower Gibbs energy, while surfaces of higher energy are sacrificed. Different crystallographic planes will have a different number of bonds per unit of area, and the bond strengths can also change according to the composition. Actually, very often when a surface energy value of a given crystalline material is indicated, it is in fact an average of the surface energy of the different crystalline faces. Taking as example a face-centered cubic lattice, when increasing the Miller indices, typically the atomic density of the planes decreases. The exception is that in the plane family [1 1 1], which contains six nearest neighbors, three bonds for each surface atom have to be broken when cutting the crystal along such direction, while for [1 0 0] and [1 1 0] planes, with lower atomic density, four and six bonds have to be broken, respectively [22]. Therefore, the surface energy of the former planes is larger relatively to the [1 1 1] plane family. Planes with the highest density have a lower surface energy and rate of growth, and therefore the final morphology of the crystal growth will be defined by the high-density atomic planes [21, 22]. However, several studies have indicated that a spherical morphology, which is the configuration that minimizes the surface area, is energetically more favorable for solids at high temperatures, and the difference of surface energy between different crystallographic planes becomes a less important factor [22].

2.3. Electrical and dielectric properties

In this section, we will start to address the electrical properties of LN single crystalline and polycrystalline. Afterward, we will address polycrystalline LN. However, for both cases, it is important to analyze the properties for different temperature ranges and different stoichiometries, since both parameters have influence on the mechanisms of electrical conduction.

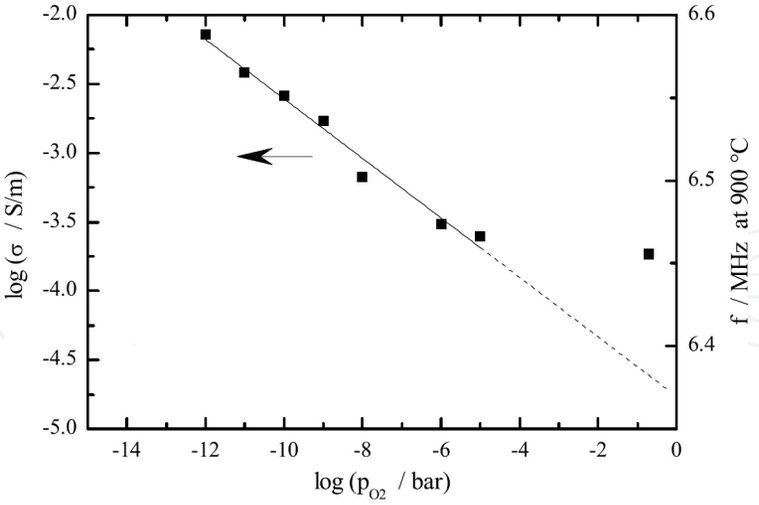

Figure 10. Dependence of a LN stoichiometric sample (sample 3 of **Figure 12**) total electrical conductivity with the oxygen partial pressure p_0, at 1173 K (900°C). The solid line is the linear fit of the experimental values, while the dotted line is the extrapolation [6].

It is well known that the electrical conductivity of LN single crystals, as well as some optical properties, is strongly dependent on the surrounding environmental characteristics, in

particular the partial oxygen pressure p_0, as well as the Li/Nb ratio (stoichiometry). It was demonstrated that the electrical conductivity in high temperature ranges, between 600 and 1300 K, has a dependency of the type $p_0^{-1/4}$ for low $p_0 \lesssim 1$ torr (1 torr ≈ 1/760 of a standard atmosphere). **Figure 10** presents the dependence of a sample with [Li]/[Nb] = 1 (sample 3; see inset table of **Figure 12**) total electrical conductivity with p_0, at 1173 K (900°C) [6]. The solid line, which represents the linear fit of the experimental values, has a slope of approximately ¼ [6].

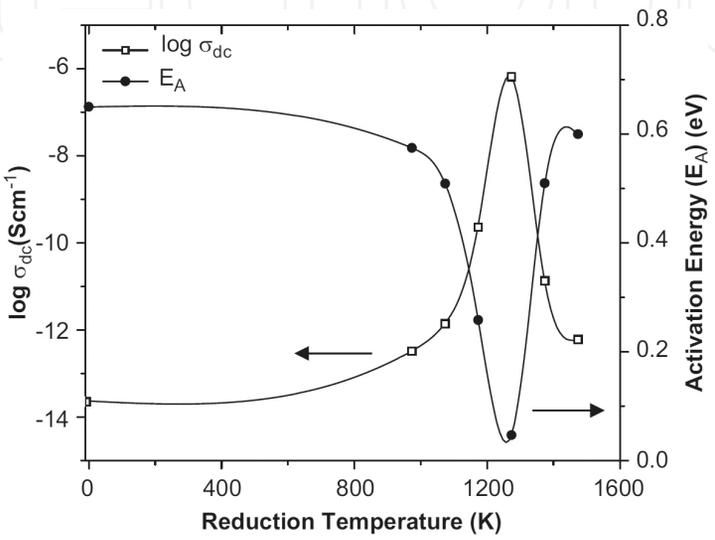

Figure 11. Dependence of σ_{dc} and E_A at room temperature with reduction temperature for different reduced congruent LN single crystals [23].

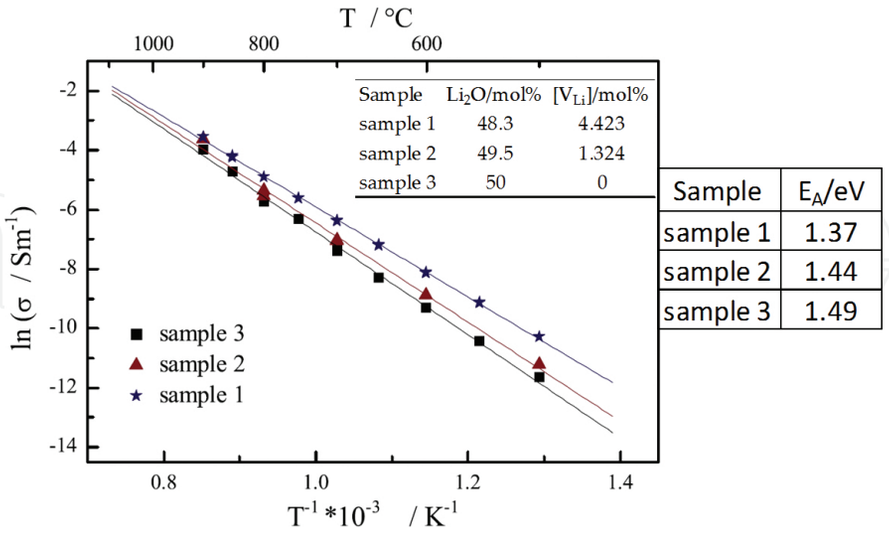

Figure 12. Arrhenius representation of the electrical conductivity of single-crystalline LN samples with different lithium contents, in the temperature range between 500 and 900°C. [V_{Li}] represents the mol% of lithium vacancies, calculated through the lithium vacancy model (Eq. (1)). The activation energies (E_A) for the different samples are also indicated (adapted with permission from [6]).

http://dx.doi.org/10.5772/64395

The electrical properties of LN are conditioned by the oxidation or reduction atmosphere, during thermal annealing: in a low p_0 ($\lesssim$1 torr) environment, it will consist of a reducing atmosphere. The effects of a reducing atmosphere on LN crystals are typically referred in the literature to originate the following modifications: the first is loss of oxygens from the structure, which leads to the release of electrons which are trapped by Nb^{5+} cations, consequently originating Nb^{4+} cations; the second is that the reducing atmosphere leads to the diffusion and loss of lithium cations, creating more lithium vacancies and an excess of niobium cations relatively to lithium, thus leading to the occupation of Li^{+} lattice sites by the Nb^{5+} species (the so-called anti-site niobium defects Nb_{Li}), according to the lithium vacancy model, presented in Eq. (1) [6, 23]. Dhar et al. studied the low temperature (77–373 K) dependency of dc electrical conduction in reduced congruent LN single crystals [23]. The samples had different levels of oxygen reduction according to the temperature of reduction, in a vacuum of approximately 10^{-5} mbar. **Figure 11** shows the dependence of the dc conductivity (σ_{dc}) and activation energy (E_A) at room temperature with the reduction temperature for different samples [23].

The presence of a maximum in σ_{dc} and a minimum in E_A can be explained by the Mott's variable range hopping (VRH) mechanism: the oxygens released during reduction can produce free electrons according to Eqs. (8) and (9) [23]:

$$2Nb^{5+} + O^{2-} \leftrightarrow 2Nb^{4+} + O_v^{2-} + 1/2O_2 \tag{8}$$

and

$$Nb^{4+} \leftrightarrow Nb^{5+} + e^{-} \tag{9}$$

and therefore the release of oxygen during reduction originates free electrons that can get trapped in niobium ions, and the conduction mechanism is assigned to polaronic hopping between Nb^{5+} and Nb^{4+} cations [23]. The maximum and minimum observed in **Figure 11** can be explained according to the ratio of Nb^{4+}/Nb^{5+} states: for low reduction temperatures, few Nb^{4+} states will be created, while for high reduction temperatures, Nb^{4+} will predominate. However, for intermediate reduction temperature, there will be a case where we will get Nb^{4+}/Nb^{5+} = 0.5. In that case, a maximum in the conductivity and a minimum in E_A are to be expected, because the different oxidation states through which the polaronic hopping occurs are closer to each other [23]. They also concluded that actually the reduction annealing in low p_0 does not lead to a significant loss of lithium ions, as it was aforementioned (and is frequently mentioned in the literature), because they have shown that when reheating the reduced samples in an oxygen-rich atmosphere, without any content of lithium vapor, the conductivity decreases and regains practically the same value as unreduced samples, which imply that annealing at low p_0 does not have an important role in lithium loss [23]. For a polaronic VRH, the conductivity has a dependency as expressed in Eq. (10):

$$\sigma_{dc} = \sigma_0 exp\left[-\left(\frac{T_0}{T}\right)^{s}\right] \tag{10}$$

where σ_0 is the pre-exponential factor, T_0 is Mott's characteristic temperature, and s is the exponent for the VRH model. For reduced LN single crystals, the exponent s = ¼ is the one which better describes the temperature dependency of σ_{dc} (check on [23] to see a $\log(\sigma_{dc})$ vs $T^{-1/4}$ plot).

For higher temperature ranges, in reduced LN single crystals, the VRH of polarons continues to be one of the mechanisms for the electrical conduction. However, and especially for congruent samples, lithium diffusion starts to be thermally activated, and when increasing the temperature, the main contribution for the total electrical conductivity may become ionic, assigned to lithium diffusion through lithium vacancies in the network (once again, we recall the lithium vacancy model) [6]. **Figure 12** shows the Arrhenius representation of the total electrical conductivity of LN single-crystalline samples with different lithium oxide molar percentages, in the temperature range between 773 and 1173 K [6]. The conductivity increases with the decrease of the Li_2O content, indicating the influence of lithium diffusion through lithium vacancies. The ionic conductivity will be larger for congruent LN, because the density of lithium vacancies is larger.

With respect to the frequency dependency of the electrical properties, typically studied by means of impedance spectroscopy (IS), some results of the work done by Mansingh and Dhar will be addressed, namely, those related with the ac electrical conductivity (σ_{ac}) and the dielectric constant (ε') of congruent LN single crystals [24]. This work was published in 1985; however, more recent papers reporting dielectric studies as a function of frequency and temperature for LN single crystals are surprisingly not that easy to find, because most of them deal with polycrystalline LN or with LN doped with other elements.

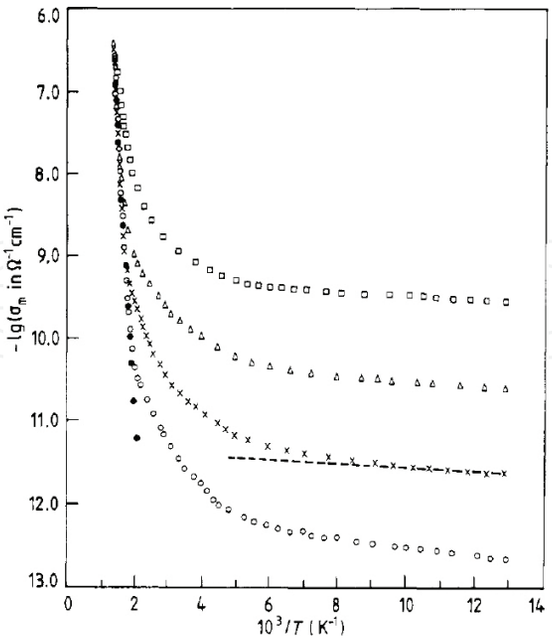

Figure 13. Dependence of σ_{ac} and σ_{dc} with the temperature (77–700 K) for different fixed frequencies (kHz): (•) DC, (○) 0.1, (x) 1, (Δ) 10, (□) 100 [24].

http://dx.doi.org/10.5772/64395

Figure 13 shows for a congruent LN single crystal the dependence of σ_{ac} and also σ_{dc} (although in a more limited temperature range relatively to σ_{ac}) with the temperature (77–700 K) for different frequencies, between 100 Hz and 100 kHz. It is visible that for lower temperatures σ_{ac} presents high-frequency dispersion, and it is considerably higher than σ_{dc}, while for higher temperatures it becomes practically frequency-independent and strongly temperature-dependent. Moreover, the temperature at which σ_{ac} starts to have the same value as σ_{dc} increases with the increase of the frequency. The mechanism for lower temperatures was found to be well described by a hopping-over-the-barrier (HOB) mechanism, and it was correlated with electron hopping between different valence states of the niobium, because of the reduction of Nb^{5+} due to oxygen deficiencies (as it was referred before) [24].

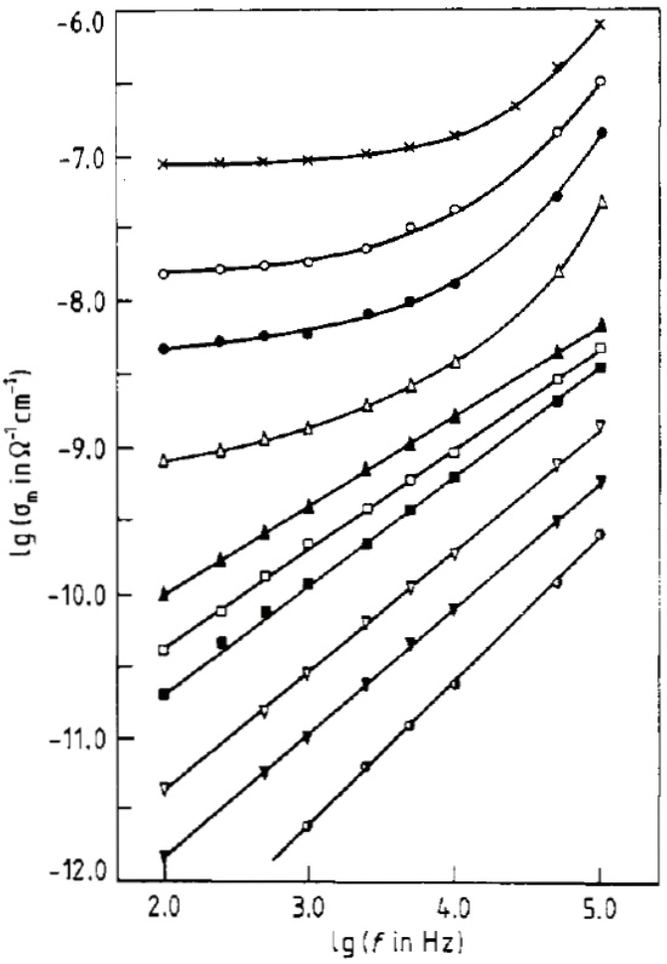

Figure 14. Frequency dependence of σ_{ac} for some fixed temperatures (K): (◑) 77, (▼) 220, (▽) 320, (■) 415, (□) 475, (▲) 530, (Δ) 580, (●) 625, (○) 650, (x) 680 [24].

Figure 14 shows the frequency dependence of σ_{ac} for some fixed temperatures. For lower temperatures, up to 530 K, the dependency of σ_{ac} with the frequency can be expressed by the relation presented in Eq. (11) [24]:

$$\sigma(\omega) = A\omega^s \tag{11}$$

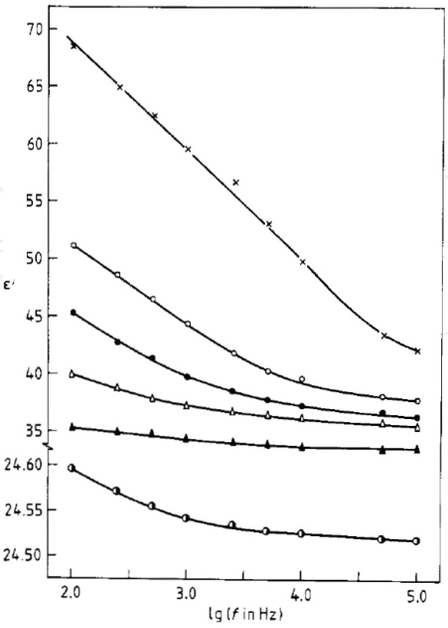

Figure 15. Frequency dependency of the dielectric constant (ε′) for different fixed temperatures (K): (◑) 77, (▲) 530, (Δ) 580, (●) 625, (○) 650, (x) 680 [24].

This is the well-known relation found by Mott and Davis which describes the frequency dependency of σ_{ac} for many amorphous and crystalline materials. The HOB mechanism presents a frequency dependency which can be described by Eq. (11). Furthermore, the HOB mechanism predicts a decrease of the frequency exponent s with the increase of temperature, and the values of s calculated by Mansingh and Dhar (~1 for 77 K and ~0.6 for 530 K) agree satisfactorily with the HOB model [24]. For higher temperatures, as it was aforementioned, σ_{ac} becomes practically frequency-independent and with a magnitude close to σ_{dc}. At the same time, for the same high temperature range (relatively to σ_{ac}, see **Figure 14**), ε' is characterized by a strong frequency dispersion, as shown in **Figure 15**.

The temperature dependence of ε' for different fixed frequencies, between 100 Hz and 100 kHz, is also shown in **Figure 16**.

It can be noted in **Figure 16** that the temperature from which ε' shows a sharp increase increases with the increase of frequency. So, from the presented plots of σ_{ac} and ε', it is evident that the temperature dependences show evidence of two distinct mechanisms for the conductivity. At low temperatures, the mechanism was already identified, the HOB mechanism with a high distribution of relaxation times. For higher temperatures, the strong ε' dispersion is probably associated with the dc conduction mechanisms, while both ac and dc conductivities are determined by the same mechanism, long-range hopping of charge carriers [24]. A sample with thickness reduced to half, keeping the electrode surface area constant, was included in **Figure 16** to demonstrate that the sharp increase of ε' is not related with the electrode barriers and spatial charge accumulation at the electrode/sample interface [24].

http://dx.doi.org/10.5772/64395

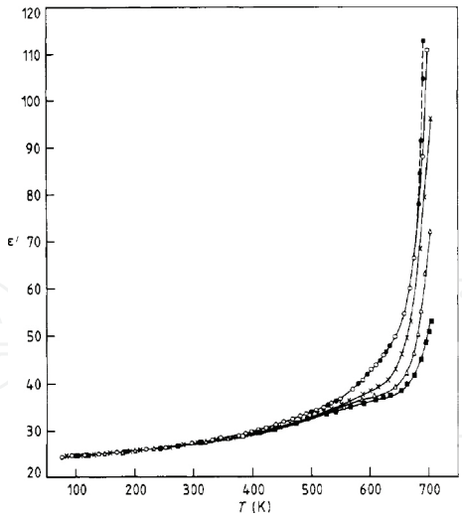

Figure 16. Temperature dependency of the dielectric constant (ε') for different fixed frequencies (kHz): (○) 0.1, (x) 1, (Δ) 10, (■) 100, (●) Sample with half of the thickness, keeping the same area [24].

We will end this section by briefly addressing the electrical and dielectric properties of polycrystalline LN. In such case, the behavior of the referred properties can reflect the presence of grain boundaries in the material. This effect of grain boundaries can be more clearly seen in IS measurements, because the characteristic frequencies (or times) at which grain boundary processes occur are different from those that occur in the bulk of the grains, and therefore Nyquist diagrams [plot of the negative of the imaginary part of the impedance, −Im(Z), in the y-axis over the real part of the impedance, Re(Z), in the x-axis] originate successive semicircles, where each point of the semicircle corresponds to a different frequency value which increases counterclockwise. Lanfredi and Rodrigues report in their work IS studies of the electrical conductivity and dielectric constant of polycrystalline LN [25]. **Figure 17** presents Nyquist diagrams for different temperatures of two polycrystalline LN samples *a* and *b*. Sample *b* has approximately half of the thickness to electrode surface area ratio (*l*/A) relatively to sample *a*.

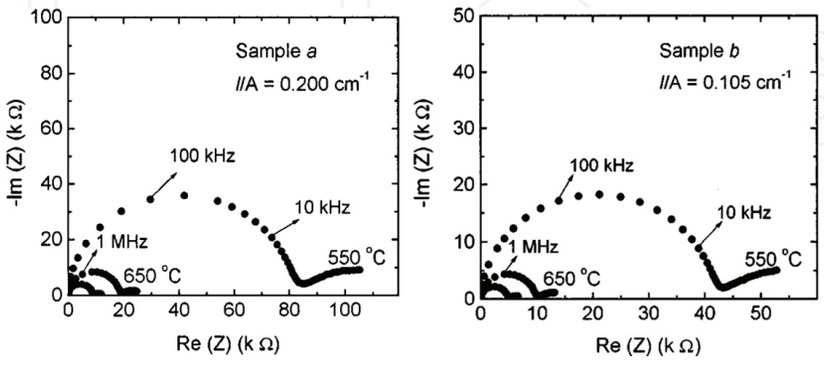

Figure 17. At left: Nyquist diagram for different temperatures for a polycrystalline LN sample with a thickness to electrode surface area ratio *l*/A = 0.200 cm^{-1} (sample *a*). At right: Nyquist diagram for different temperatures for sample *a* polycrystalline LN sample with a thickness to surface area ratio l/A = 0.105 cm^{-1} (sample *b*), approximately half of sample *a*. For both samples, the smallest semicircle corresponds to a measurement performed at 700°C [25].

Comparing both diagrams, it is visible that for the same temperature, the real part of the complex impedance Re(Z) of sample *b* is approximately half of sample *a*, thus confirming that the high-frequency semicircle is the bulk response of the samples, since the resistance is directly proportional to the path length [25]. Furthermore, the frequency value distribution in the bulk-response semicircle is the same for both samples, indicating the homogeneity of the bulk response, and that the relaxation frequency, given by the peak of the bulk semicircle (in the peak, the relation $2\pi f_0 R_b C_b = 1$ is fulfilled, where R_b and C_b are bulk resistance and capacitance, respectively), is an intrinsic property of the material and does not depend on geometrical factors [25]. As expected, the bulk resistance decreases with the increase of the temperature. The low-frequency semicircle is assigned to the response of grain boundaries, and its depressed shape is an indicator of a nonhomogeneous electrical behavior of grain boundaries [25]. This nonhomogeneous behavior can be related with an existence of a distribution of relaxation times.

The complex impedance semicircle for the bulk response can be well fitted by simple R_bC_b equivalent circuit. A bulk electrical conductivity σ_b can be defined according to Eq. (12):

$$\sigma_b = \frac{1}{R_b}\frac{l}{A} \tag{12}$$

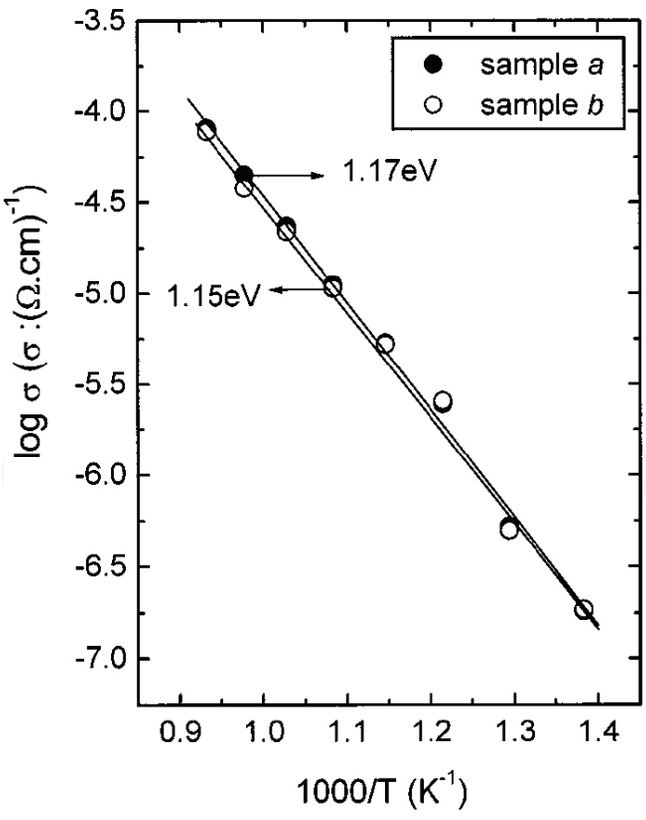

Figure 18. Arrhenius representation of the bulk electrical conductivity σ_b of the polycrystalline LN samples *a* and *b*, in the temperature range between 450 and 800°C [25].

http://dx.doi.org/10.5772/64395

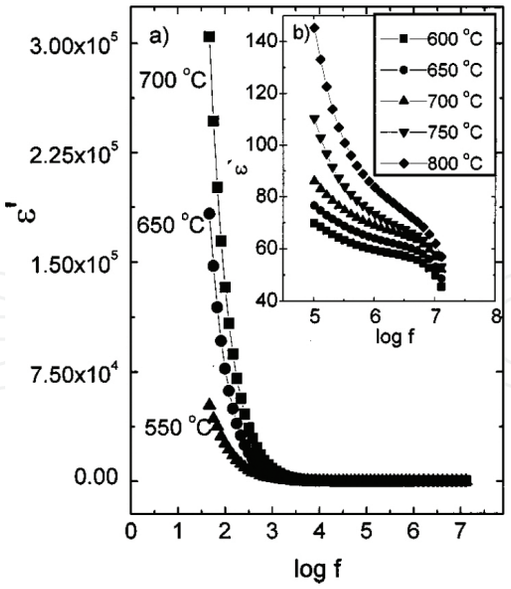

Figure 19. Frequency dependency, in the range of 5–10^7 Hz, of ε' for some fixed high temperatures, for sample *b* [25].

R_b can be determined through the Nyquist plots by the second interception (just before the grain boundary response) of the bulk semicircle with the real axis. **Figure 18** displays for both samples *a* and *b* the Arrhenius representation of σ_b in the temperature range between 450 and 800°C [25]. The activation energies are very similar.

To conclude this section, it is included in **Figure 19** the frequency dependency, between 5 and 10^7 Hz, of ε' for some fixed high temperatures, for sample *b*.

For lower frequencies, a strong dispersion of ε' is observed. This is due to spatial charge accumulation at the grain boundaries, and the charge accumulation at interface electrode/sample may also contribute to the sharp increase of ε' for lower frequencies. This behavior is often observed for polycrystalline materials.

2.4. Case study: preparation and characterization of polycrystalline LN by the Pechini method

2.4.1. Preparation process: the Pechini route

The sol-gel process is a well-known route for the synthesis of different types of materials, and in its basic description, it can be referred as a technique that synthesizes a solid compound through a chemical reaction in solution at low temperatures. There are different sol-gel methodologies according to the type of precursors used and the chemical reactions leading to the formation of the gel: there is the sol-gel methodology based on the hydrolysis-condensation of metal alkoxides, the "chelate-gel" route, involving aqueous solutions containing metal chelates, and the Pechini route. The sol-gel methodologies have general advantages such as the very good control of the stoichiometry and purity of the final material, low processing temperatures, possibility, and good flexibility in developing thin films as well as the possibility

to have control over some important characteristics, such as the size and shape of the particles and homogeneity.

The Pechini route takes its name on its developer, Maggio Pechini in 1967 [26]. In particular, it was developed to include metals which are not suitable for traditional sol-gel reactions due to their unfavorable hydrolysis equilibria, and thus this method has the advantage of not requiring that the metallic species involved form stable hydroxo-complexes. This method is known for its use on the synthesis of multicomponent metal oxide materials [26], and basically this method uses an R-hydroxycarboxylic acid, such as citric acid (CA), to lead the formation of stable metal complex, i.e., the metallic cations of interest form stable complexes known as chelates. After this step, a polyalcohol, such as ethylene glycol (EG), is used to promote the polyesterification of the chelates, leading to the formation of a polymeric resin, where the metallic cations are trapped in the organic polymeric network. In other words, the polyalcohol is able to create links between the chelates by polyesterification reactions. The formation of the polymeric resin results in the formation of the gel. The subsequent drying process leads to the pyrolysis of the organic compounds, resulting in the formation of multicomponent metal oxide [26].

In this case study, the precursors lithium nitrate ($LiNO_3$) and niobium chloride ($NbCl_5$) (purity > 99%) were chosen. A molar ratio of 1:1 between $LiNO_3$ and $NbCl_5$ was established in order to enhance the formation of the $LiNbO_3$ stoichiometric phase. Firstly, the $LiNO_3$ and $NbCl_5$ were dissolved in deionized water and in a hydrogen peroxide solution (H_2O_2, 3%, V/V), respectively. For each gram of $NbCl_5$, 3.2 ml of H_2O_2 was used, originating a yellow transparent and clear solution. Both precursor solutions were mixed with citric acid (CA), fixing a molar ratio of 1:1 between the CA and the metallic cations, in order to form the metal complexes (chelates). The mixing was performed using a magnetic stirrer for 30 min at room temperature. After the mixing process, ethylene glycol (EG) was added to promote the polyesterification of the chelates. A mass ratio of 2:3 was established between the CA and EG to determine the quantity of EG to use. The final solution was mixed again with a magnetic stirrer for about 3 h, and the final gel was yellow and transparent, maintaining its macroscopic appearance for a long time period (>1 month). **Figure 20** outlines the entire preparation process.

The base powder was obtained after drying the gel at 300°C for 1 h, with a heating ramp of 5°C/min, yielding a black/grayish powder.

2.4.2. Thermal, structural, and morphological properties

The base powder was subjected to several heat treatments (HTs) at temperatures between 400 and 1000°C. These temperatures were chosen according to the differential thermal analysis (DTA) results, presented in **Figure 21**. This thermal technique was performed between room temperature and 1200 °C using a Linseis 63A apparatus. The heating rate was 20 °C/min and Al_2O_3 powder as used as reference. In **Figure 21**, the thermogram shows the presence of three exothermic thermal processes at the temperatures of 490, 790, and 1050°C, approximately. Consequently, HTs were performed at 450, 500, 800, and 1000°C, for 4 h.

http://dx.doi.org/10.5772/64395

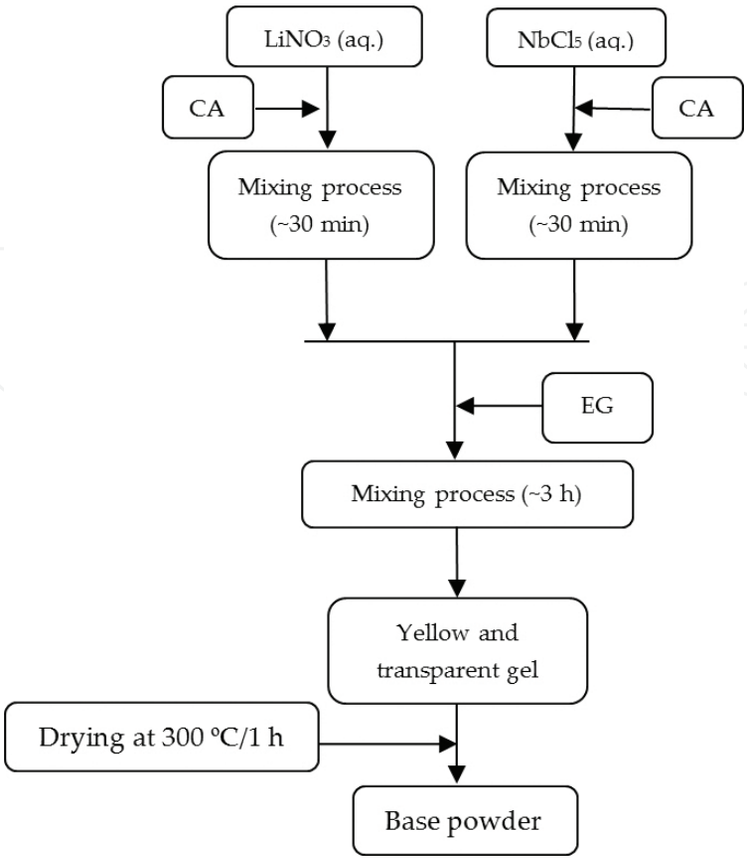

Figure 20. Diagram of the Pechini method used for the synthesis of the LN base powder. CA, citric acid; EG, ethylene glycol.

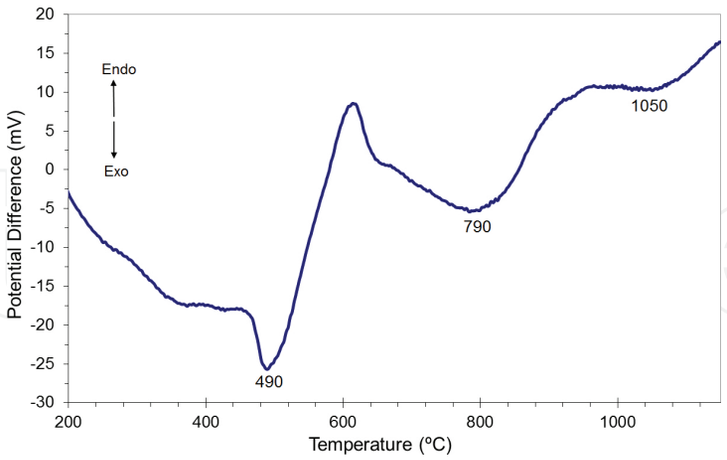

Figure 21. DTA thermogram of the base powder synthesized by the Pechini method. This thermal analysis was performed between room temperature and 1200 °C, with a heating rate of 20 °C/min.

The XRD measurements performed on these powders (not shown here) revealed that for the HT at 500°C, the LN and $LiNb_3O_8$ crystalline phases are present and that the increase of the HT temperature promotes the development of the $LiNb_3O_8$ phase. However, the powder HT

at 450°C only contained the $LiNbO_3$ phase, whereby this powder was used to prepare pellets which were then sintered at 450°C for 4, 12, 24, 48, and 96 h. Thirty milligrams of powder was used for the preparation of the 10-mm diameter pellets, resulting in a thickness of about 1 mm when applying a uniaxial pressure of 1.5 tons. Hereafter, we will refer to these pellets as samples.

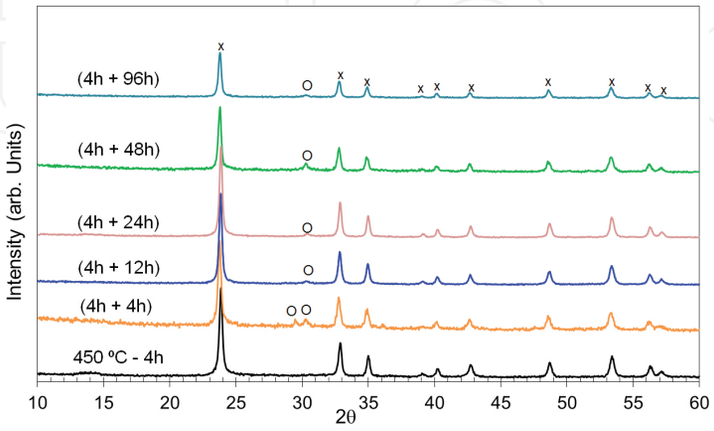

Figure 22. XRD patterns of the base powder HT at 450°C and of the samples sintered for 4, 12, 24, 48, and 96 h (× $LiNbO_3$; O $LiNb_3O_8$).

Figure 22 depicts the XRD patterns of the samples sintered during the aforementioned time intervals. The patterns show that the sintering process activated the formation of the $LiNb_3O_8$ phase. The XRD technique was performed on a Philips X'Pert MPD (CuK_α radiation, λ = 1.54056 Å), with a step 0.02° in 1 s, in the 2θ angle range of 10–60°. The identification of the crystalline phases was made using the database of the Joint Committee on Powder Diffraction Standards–International Center for Diffraction Data. To get a further insight about the contents of each phase in the samples as well as to calculate the crystallite sizes associated with each phase, a Rietveld refinement was performed for all the diffraction patterns shown in **Figure 22**, using the PowderCell software. In **Figure 23**, the Rietveld fits of the samples 4 h and 4 h + 96 h are presented.

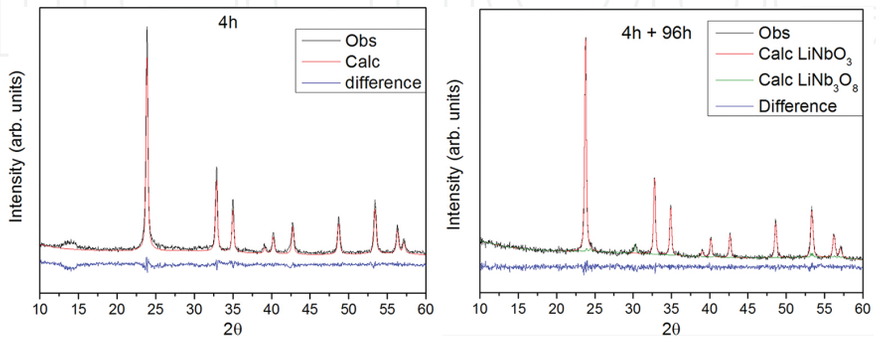

Figure 23. The Rietveld fits of the XRD patterns for the powder HT at 450°C, containing only the LN crystalline phase and the sample sintered for 96 h, containing both LN and $LiNb_3O_8$.

http://dx.doi.org/10.5772/64395

The Rietveld fit parameters indicate a good fit of the structural models to the experimental data (**Table 2**). Although the XRD patterns shown in **Figure 22** may suggest that the $LiNb_3O_8$ phase is present in small amounts, the mass percentages shown in **Table 2** show that the presence of this phase is relevant, reaching the maximum value for the sample 4 h + 96 h. In fact, both LN and $LiNb_3O_8$ have reflections lying in close diffraction angles, and some of the observed peaks contain a contribution of the $LiNb_3O_8$ phase, besides the LN phase, explaining the relatively high mass percentages. The crystallite size of both phases stands approximately constant for the different samples, especially for the $LiNb_3O_8$ phase, which has larger sizes relatively to the LN phase.

Sample	R_{wp}	R_{exp}	χ^2	Crystallite size (nm)		Mass%		ε'	tan δ
				$LiNbO_3$	$LiNb_3O_8$	$LiNbO_3$	$LiNb_3O_8$		
4 h	8.78	6.20	2.01	43.90	–	100	–	–	–
4 h + 4 h	10.40	8.72	1.42	45.52	61.94	72.48	27.52	8.64	0.06
4 h + 12 h	6.26	4.77	1.72	48.30	61.32	66.48	33.52	9.37	0.05
4 h + 24 h	6.31	4.49	1.97	50.23	61.03	66.94	33.06	16.85	0.09
4 h + 48 h	9.72	8.23	1.39	44.84	62.28	75.90	24.10	16.36	0.13
4 h + 96 h	9.37	7.70	1.48	46.65	59.50	61.76	38.24	13.06	0.18

Table 2. The initial three parameters are the weighted profile *R*-factor (R_{wp}), the expected *R*-factor (R_{exp}), and the "chi squared" χ^2. The crystallite size and mass percentage of each crystalline phase in all the samples are also indicated. The last two columns show the dielectric constant (ε') and loss tangent (tan δ) at 10 kHz and room temperature (300 K).

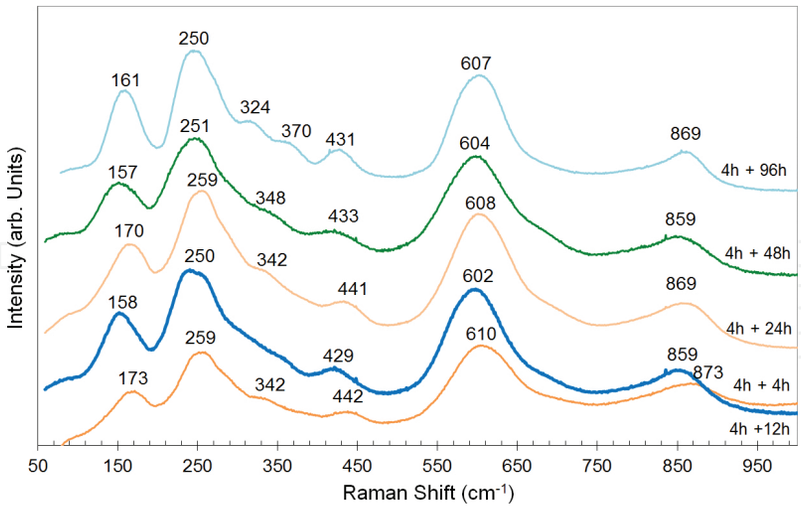

Figure 24. The Raman spectra of the samples sintered for different times between the time range 4 and 96 h, performed at room temperature.

In **Figure 24**, the Raman spectra of the sintered samples are presented. The spectra show the presence of vibrational bands which are the result of an overlapping of vibrational models of LN and also of the $LiNb_3O_8$ crystalline phase, as a consequence of the polycrystalline structure

of the prepared samples. For a further analysis of the LN and $LiNb_3O_8$ vibrational modes, the authors suggest the reading of Bartasyte et al. report [27]. The room-temperature Raman spectroscopy was performed in backscattering geometry using a T64000 Jobin-Yvon spectrometer. A microscope objective (50×) focused the exciting light (Ar^+ laser, λ = 532 nm) onto the sample (spot diameter <0.8 μm).

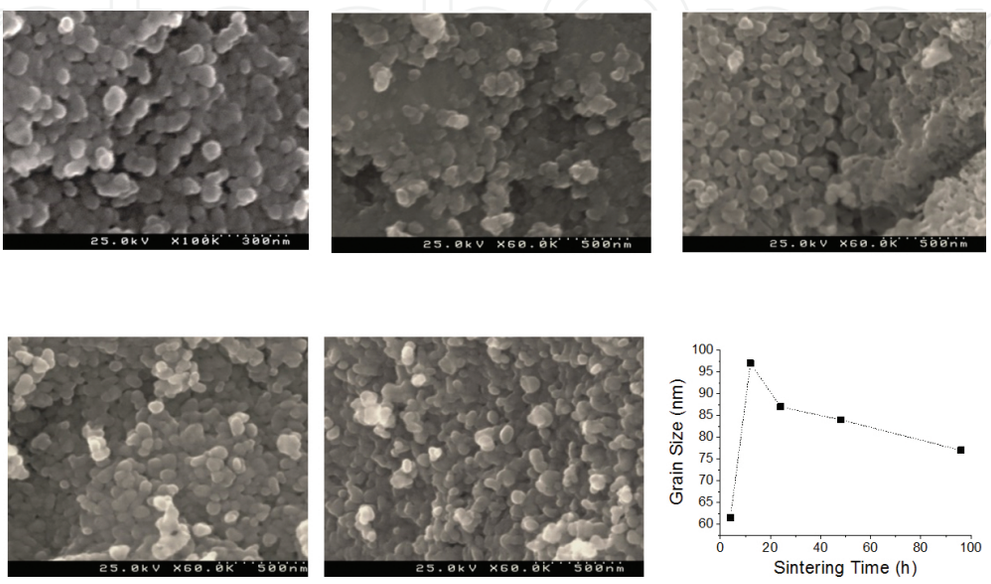

Figure 25. SEM micrographs of the LN polycrystalline samples prepared by the Pechini method, sintered at 450°C for 4, 12, 24, 48, and 96 h.

In **Figure 25**, SEM micrographs of the samples are shown, as well as the variation of the grain size with the sintering time. The grain size increases significantly with the sintering time from 4 to 12 h and then decreases slightly up to 96 h. As for the morphology, the grains show an approximate spherical geometry. The SEM was executed on a HITACHI S4100-1. All samples were sputtered with carbon before the analysis.

2.4.3. Electrical and dielectric properties

The electrical analysis of these types of samples is not evident. **Figure 26** shows the temperature dependence of the dc conductivity (σ_{dc}) for all samples, revealing a decrease of the conductivity with the increase of the sintering time. This suggests a probable decrease in the number of charge carriers.

However, **Figure 27** shows that the activation energy, calculated in the high-temperature region (marked by the Arrhenius regression line in **Figure 26**), decreases substantially from sample sintered at 4 h to the sample sintered at 96 h. This profile indicates that the height of the potential barriers, from which the charge carriers must pass through, decreases, which should promote an increase in their mobility. Therefore, this analysis indicates a decrease in the number of charge carriers and also an increase in their mobility.

http://dx.doi.org/10.5772/64395

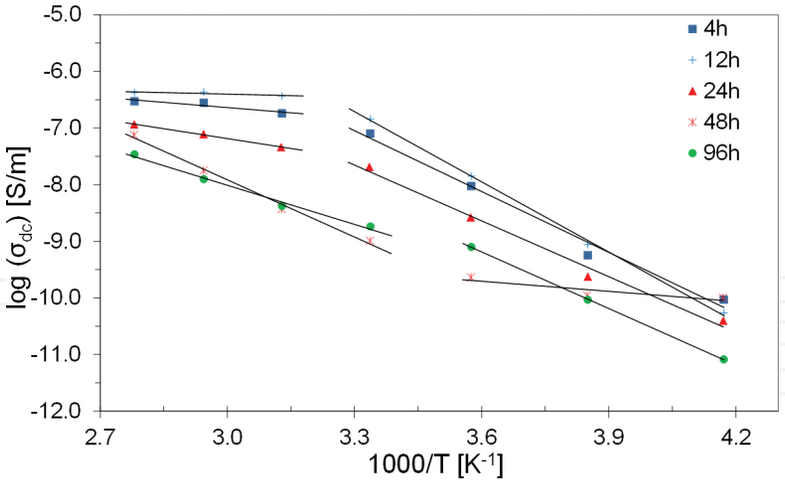

Figure 26. Arrhenius representation of the dc conductivity (σ_{dc}) for the samples sintered at 450°C for 4, 12, 24, 48, and 96 h.

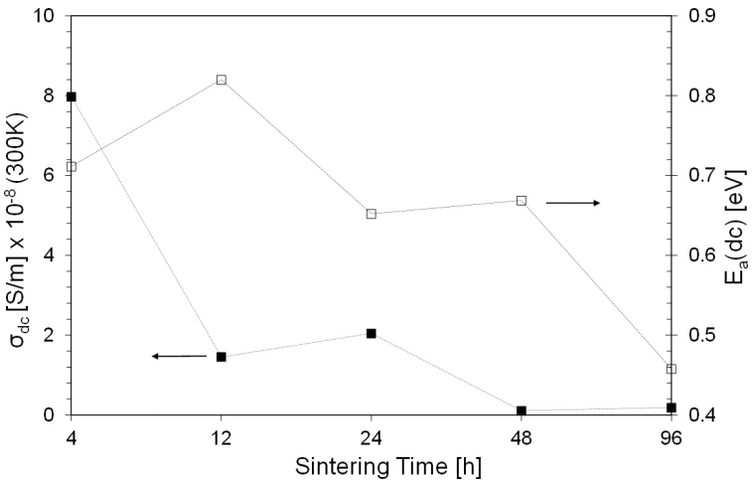

Figure 27. Dc conductivity (σ_{dc}) and activation energy (E_a(dc)) of the samples sintered at 450°C for 4, 12, 24, 48, and 96 h, at room temperature (300 K).

As discussed in Section 2.3, the electrical conduction in crystalline LN can be due to oxygen vacancies, in low-pressure and/or high-temperature conditions (polaron-hopping mechanism), and due to lithium ions in high-pressure conditions (ionic conduction). In this case, the conduction will depend on the ratio between Li/Nb both for high and low pressures. Therefore, in this case context, the conduction related with the lithium-ion (Li^+) hypothesis seems to be more relevant. The existence of the $LiNb_3O_8$ secondary phase, which is a reach niobium LN phase, implies an increase of the number of Li^+ ions not connected to a crystalline structure, which allied to the decrease of the activation energy should improve the σ_{dc}, which is not observed. This fact indicates that the number of Li^+ ions inserted in the crystalline structure increases and is explained by two hypotheses: there is a possible existence of an amorphous phase in all samples and thus the number of lithium ions inserted in this amorphous phase

should decrease with the increase of the sintering time, stimulating an increase of the crystalline amount. The second hypothesis is associated with the low-melting point of lithium (~454 K). The increase of the sintering time must raise the possibility of some Li^+ ions to be released during sintering. Density measurements revealed that all samples have a density between 3.53 and 3.69 g/cm^3, which are values lower than the characteristic ones for LN (4.65 g/cm^3) and $LiNb_3O_8$ (3.87 g/cm^3). This fact increases the probabilities of the first hypothesis.

Both dc and ac conductivities (**Figures 26–29**) increase with the rise of the measurement temperature, showing that both mechanisms are thermally activated. However, with the increase in the sintering time, the σ_{ac} shows the opposite trend of σ_{dc} (it increases). This indicates that the conduction mechanism and dominant charge carriers are not the same in both processes. In our opinion, the σ_{ac} increase should be related with the decrease of the grain size (**Figure 25**) observed from sample sintered at 12 h up to the sample sintered at 96 h.

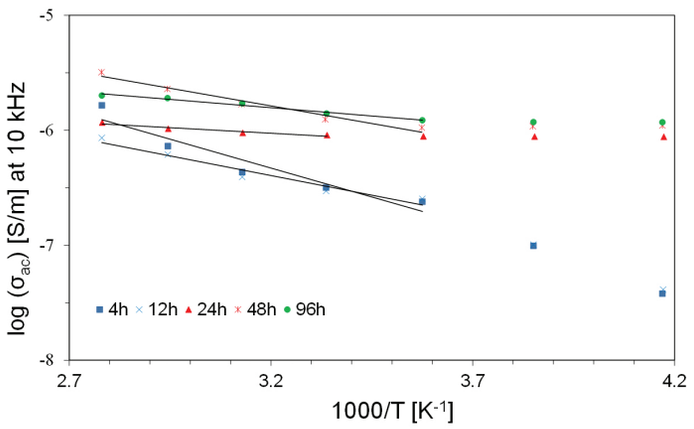

Figure 28. Arrhenius representation of the ac conductivity (σ_{ac}) for the samples sintered at 450°C for 4, 12, 24, 48, and 96 h.

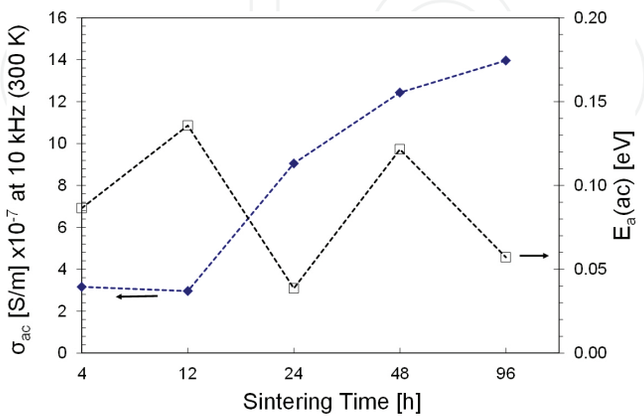

Figure 29. Ac conductivity (σ_{dc}) and activation energy (E_a(ac)) of the samples sintered at 450°C for 4, 12, 24, 48, and 96 h, at 10 kHz and room temperature (300 K).

http://dx.doi.org/10.5772/64395

The dielectric constant is maximum for the sample sintered at 24 h (**Table 2**), measured at room temperature and 10 kHz, which is in accordance with the Rietveld refinement results (**Table 2**), by presenting the highest crystallite size. The sample sintered at 48 h shows a dielectric constant value very near the maximum, which should be related with the amount of LN phase present in the sample and not the size of their grains (**Table 2**). It must be noted that the values presented in **Table 2** were obtained without assuming the existence of the hypothetical amorphous phase. These two samples present a dielectric loss below 0.15 at room temperature and 10 kHz (**Table 2**), being almost constant for temperatures between 200 and 300 K.

The 3D plots (**Figures 30** and **31**) show the presence of a dielectric relaxation phenomenon practically independent on the measurement temperature. However, the frequency of the maximum observed in the loss tangent diagram decreases with the increase of the sintering time, which can be related to the suggested decrease of the amorphous phase content and consequent increase of the LN in crystalline form which is a material where the dielectric depolarization is very difficult, i.e., high-relaxation time characteristic.

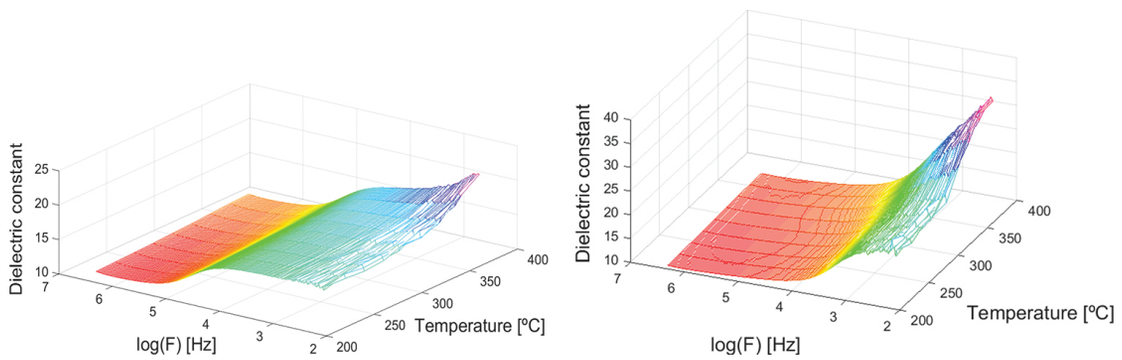

Figure 30. At left: dependency of the dielectric constant with the temperature and frequency for the sample sintered at 450°C for 24 h. At right: dependency of the dielectric constant with the temperature and frequency for the sample sintered at 450°C for 96 h.

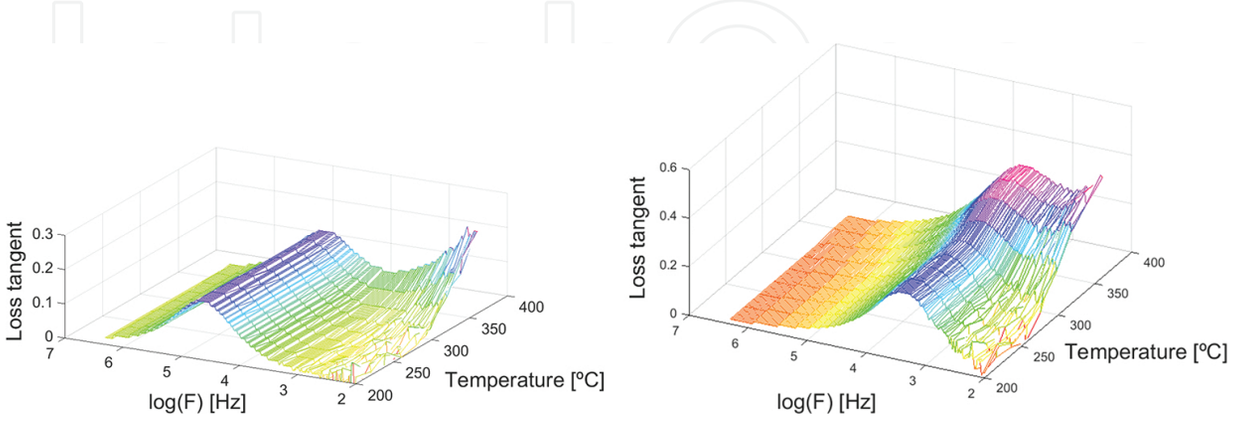

Figure 31. At left: dependency of the loss tangent with the temperature and frequency for the sample sintered at 450°C for 24 h. At right: dependency of the loss tangent with the temperature and frequency for the sample sintered at 450°C for 96 h.

Author details

Pedro R.S. Prezas* and Manuel P.F. Graça

*Address all correspondence to: pedro.rafael@ua.pt

University of Aveiro/I3N—Physics Department, Aveiro, Portugal

References

[1] Abouelleil M.M. and Leonberger F.J., *Waveguides in lithium niobate*, J. Am. Ceram. Soc., 1989, 72(8):1311-1321

[2] Graça M.P.F. and Valente M.A. *Glass ceramics with para, anti or ferroelectric active phases*, Advances in Ceramics – Electric and Magnetic Ceramics, Bioceramics, Ceramics and Environment, Prof. Sikalidis C. (Ed.), InTech (2011). Janeza Trdine 9, 51000 Rijeka, Croatia, ISBN: 978-953-307-350-7.

[3] Volk T. and Wohlecke (2008), Lithium Niobate: Defects, Photorefraction and Ferroelectric Switching, Springer-Verlag, Berlin, Heidelberg, ISBN: 978-3-540-70765-3.

[4] Bordui P.F., Norwood R.G., Jundt D.H., Fejer M.M., *Preparation and characterization of off-congruent lithium niobate crystals*, J. Appl. Phys., 1992, 71(2):875-879

[5] Kitamura K., Yamamoto J.K., Iyi N., Kimura S., Hayashi T., *Stoichiometric $LiNbO_3$ single crystal growth by double crucible Czochralski method using automatic powder supply system*, J. Cryst. Growth, 1992, 116:327-332

[6] Weidenfelder A., Shi J., Fielitz P., Borchardt G., Becker K.D., Fritze H., *Electrical and electromechanical properties of stoichiometric lithium niobate at high-temperatures*, Solid State Ionics, 2012, 225:26-29

[7] Szaller Zs., Péter Á., Polgár K., Szabó Gy., *High temperature top seeded solution growth of stoichiometric lithium niobate $LiNbO_3$ (sLN) with planar interface*, J. Cryst. Growth, 2012, 360:181-184

[8] Damjanovic D., *Materials for high temperature piezoelectric transducers*, Curr. Opin. Solid State Mater. Sci., 1998, 3(5):469-473

[9] Ohlendorf G., Richter D., Sauerwald J., Fritze H., *High-temperature electrical conductivity and electromechanical properties of stoichiometric lithium niobate*, Diff. Fundam., 2008, 8:6.1-6.7

[10] Kamali A.R. and Fray D.J., *Preparation of lithium niobate particles via reactive molten salt synthesis method*, Ceram. Int., 2014, 40:1835-1841

[11] Graça M.P.F., Prezas P.R., Costa M.M., Valente M.A., *Structural and dielectric characterization of $LiNbO_3$ nano-size powders obtained by Pechini method*, J. Sol-Gel Sci. Technol., 2012, 64:78-85

[12] Howlader M.M.R., Suga T., Kim M.J., *Room temperature bonding of silicon and lithium niobate*, Appl. Phys. Lett., 2006, 89:031914

[13] Rahn J., Hüger E., Dörrer L., Ruprecht B., Heitijans P., Schmidt H., *Self-diffusion of lithium in amorphous lithium niobate layers*, Z. Phys. Chem., 2012, 226(5-6):439-448

[14] Sanna S. and Schmidt W.G., *Ferroelectric phase transition in $LiNbO_3$: insights from molecular dynamics*, IEEE Ultrason. Ferr., 2012, 59(9):1925-1928

[15] Scrymgeour D.A., Gopalan V., Itagi A., Saxena A., Swart P.J., *Phenomenological theory of a single domain wall in uniaxial trigonal ferroelectrics: lithium niobate and lithium tantalite*, Phys. Rev. B, 2005, 71(18):184110-1/13

[16] Heitjans P., Masoud M., Feldhoff A., Wilkening M., *NMR and impedance studies of nanocrystalline and amorphous ion conductors: lithium niobate as a model system*, Faraday Discuss., 2007, 134:67-82

[17] Kitabatake M., Mitsuyu T., Wasa K., *Structure and dielectric properties of amorphous $LiNbO_3$ thin films prepared by a sputtering deposition*, J. Appl. Phys., 1984, 56:1780-1784

[18] Ridah A., Bourson P., Fontana M.D., Malovichko G., *The composition dependence of the Raman spectrum and new assignment of the phonons in $LiNbO_3$*, J. Phys.: Condens. Matter., 1997, 9(44):9687-9693

[19] Schlarb U., Klauer S., Wesselmann M., Betzler K., Wöhlecke M., *Determination of the Li/Nb ratio in lithium niobate by means of birefringence and Raman measurements*, Appl. Phys. A, 1993, 56(4):311-315

[20] Damen T.C., Porto S.P.S., Tell B., *Raman effect in zinc oxide*, Phys. Rev., 1966, 142(2): 570-574

[21] Zhan J., Liu D., Du W., Wang Z., Wang P., Cheng H., et al., *Synthesis and characterization of high crystallinity, well-defined morphology stoichiometric lithium niobate nanocrystalline*, J. Cryst. Growth, 2011, 318(1):1121-1124

[22] Stølen S. and Grande T. (2005), *Chemical Thermodynamics of Materials: Macroscopic and Microscopic Aspects*, Wiley, Hoboken, NJ, ISBN: 978-0-471-49230-6

[23] Dhar A., Singh N., Singh R.K., Singh R., *Low temperature dc electrical conduction in reduced lithium niobate single crystals*, J. Phys. Chem. Solids, 2013, 74(1):146-151

[24] Mansingh A. and Dhar A., *The ac conductivity and dielectric constant of lithium niobate single crystals*, J. Phys. D: Appl. Phys., 1985, 18(10):2059-2071

[25] Lanfredi S. and Rodrigues A.C.M., *Impedance spectroscopy study of the electrical conductivity and dielectric constant of polycrystalline $LiNbO_3$*, J. Appl. Phys., 1999, 86(4):2215-2219

[26] Roque-Malherbe R.M.A. (2009), *The Physical Chemistry of Materials: Energy and Environmental Applications*, CRC Press, 6000 Broken Sound Parkway, NW Suite 300 Boca Raton, FL 33487, United States, ISBN: 9781420082722.

[27] Bartasyte A., Plausinaitiene V., Abrutis A., Stanionyte S., Margueron S., Boulet P., et al., *Identification of $LiNbO_3$, $LiNb_3O_8$ and Li_3NbO_4 phases in thin films synthesized with different deposition techniques by means of XRD and Raman spectroscopy*, J. Phys.: Condens. Matter., 2013, 25(20):205901.

IntechOpen